RESEARCH ARTICLE

Influence of Europium Doping on the Crystallization, Morphology, and Cathodoluminescent Properties of $PbNb_2O_6$:Eu^{3+} Phosphors

Mete Kaan Ekmekçi[*] iD

[*]Department of Chemistry, Faculty of Sciences, Marmara University, Göztepe Campus, Kadıköy, 34722, İstanbul, Turkey

Abstract: Undoped $PbNb_2O_6$ and Eu^{3+} ion doped $PbNb_2O_6$ samples were synthesized by high temperature mixed oxide method, applying a heat treatment temperature of 1250°C and an annealing time of 6 hours. In order to elucidate the structural and optical behavior of $PbNb_2O_6$:Eu^{3+} phosphors, XRD (X-ray diffraction), SEM (scanning electron microscopy), EDS (energy dispersive spectroscopy), CL (cathodoluminescence) and absoption analyses were performed. The X-ray diffraction results showed that the undoped $PbNb_2O_6$ sample crystallized in a rhombohedral symmetry while Eu^{3+} doped samples formed in orthorhombic symmetry. The morphologies of the rhombohedral and orthorhombic grains were examined by SEM-EDS. The CL spectra showed spectral profiles between 580 and 780 nm in relation to the 4f–4f transitions of Eu^{3+}. A strong emission was observed at about 620 nm, corresponding to the red color and associated with the $^5D_0 \rightarrow {}^7F_2$ transition of Eu^{3+}, while the undoped sample did not exhibit CL emission of the host which is probably due to the presence of lead in the host structure. In addition, the CL analysis results showed that the emission intensity increased with the increase of Eu^{3+} ion concentration. The increase in magnetic dipole transition caused by the electron beam radiation effect of the CL with increasing doping concentration is associated with the change of dipole moments of the Eu^{3+} doped tungsten bronze host and thus differentiating the emission spectrum. UV lamp excited photograph of undoped sample showed blue-violet color while Eu^{3+} doped phosphors with red color became more significant with increasing Eu^{3+} concentration.

INTRODUCTION

Trivalent lanthanide (Ln^{3+}) ions exhibiting 4f–4f inner-shell transitions have certain properties such as high luminescence efficiency, narrow emission line, and long decay time constant. Due to their advantages, such as reliability and environmental friendliness, they have attracted great attention as new generation solid-state lighting sources in recent years (1–9). Among these materials, trivalent europium, which is used as a dopant in the production of inorganic-based red light emitting phosphors (LEDs), is known as an effective activator due to its characteristic $^5F_0 \rightarrow {}^7F_J$ (J = 0, 1, 2, 3, 4, 5) band transitions. In addition, the Eu^{3+} is well

known for its strong luminescence in the red region of the spectrum, and also has a great advantage over other rare earth ions with an even number of 4f electrons in that the initial levels of transitions in both the absorption and luminescence spectrum are non-degenerate (10). The magnetic dipole transition of $^5F_0 \rightarrow {}^7F_1$ and the electric dipole transition of $^5F_0 \rightarrow {}^7F_2$ show emissions at wavelengths of 590–600 nm and 610–630 nm, respectively. Moreover, trivalent Eu, as a potential emission activator, provides important information about spectroscopic characterization when used as a dopant in different host structures (6-10).

Cathodoluminescence (CL) is a method used in the optical characterization resulting from the interaction of the material with an electron beam provided by an electron gun. The CL analysis can be interpreted via spectral lines that are similar to those from other luminescence techniques, and characteristically dominate the spectrum with bound excitonic states and changes from emission lines, donor-acceptor double bands, and defect-related properties (11–16).

The synthesis, structural, and optical properties of several AB_2O_6-type niobate compounds have been investigated (17-21). Among the lead-based niobates, $PbNb_2O_6$ ceramics have been studied recently for their photocatalytic (22), dielectric and piezoelectric (23), ferroelectric (24-29), and thermal properties (30). Furthermore, Ihan et al. (17, 18) investigated the photoluminescence properties of rhombohedral $PbNb_2O_6$:Eu^{3+} phosphor, as well as the thermoluminescence kinetic parameters, Judd-Ofelt analysis and radioluminescence properties of orthorhombic $PbNb_2O_6$:Eu^{3+} phosphor.

$PbNb_2O_6$ exhibits three different structures in PbO-Nb_2O_5 system. The stable forms of $PbNb_2O_6$ are the rhombohedral and tetragonal polymorphs, which occur at low and high temperatures, respectively. The rhombohedral and tetragonal are not ferroelectric and piezoelectric. The only metastable orthorhombic polymorph of $PbNb_2O_6$ is an important high-temperature piezoelectric material (30) that can act as actuators that can convert electrical pulses to motion or sensors that can convert motion/pressure pulses to electrical voltage. This actuator and sensor property of piezoelectric materials can be combined in applications in the medical and engineering

fields, for example, with the imaging technique of ultrasonography, for the diagnosis of diseases and for the structural imaging of engineering materials. $PbNb_2O_6$ with high Curie temperature is used as a rocket and automobile exhaust sensor material (31). In addition, $PbNb_2O_6$ synthesized by high temperature solid state method was evaluated in terms of lithium storage in rechargeable batteries (32, 33). The ferroelectric phase transition properties of lead meta niobate ($PbNb_2O_6$) with a single crystal under gamma rays radiation have been investigated (34). Samarium doped lead based ceramic materials with rhombohedral structure were produced by a high temperature conventional solid state synthesis and examined for their dielectric and piezoelectric properties (35). Due to investigating the tunable dielectric properties of $PbNb_2O_6$ via calcium substitution, $Pb_{1-x}Ca_xNb_2O_6$ perovskite structures were synthesized via sol-gel auto-combustion method (36). Due to the high piezoelectric constant, the high Curie temperature of Ca, and excess Ti doped high density $PbNb_2O_6$ (PN), ferroelectric ceramics produced by the traditional powder synthesis method and their use in ultrasonic applications as piezoelectric material have been investigated (37). $PbNb_2O_6$ ferroelectric ceramics with orthorhombic structure have been synthesized by solid state reaction route and evaluated in terms of their dielectric properties in the frequency range of 20 Hz to 2 GHz (38).

Undoped and Eu^{3+} doped $PbNb_2O_6$ ceramic phosphors have been synthesized via solid state synthesis. The structural and cathodolumi-nescence properties of the samples were investigated. In addition, the effect of europium doping on the crystallization, morphology, structural and cathodolumi-nescence properties of the samples has also been researched and evaluated. The microphase morphology, crystalline structure and cathodoluminescence properties of the samples were carried out by XRD, SEM, EDS, CL, and absorption analyses.

EXPERIMENTAL SECTION

Undoped $PbNb_2O_6$ and Eu^{3+} doped $PbNb_2O_6$:xEu^{3+} (x = 0.5, 1, 3, and 6 mol%) samples were produced by using the solid state reaction route, where x represents 2 atomic value due to Eu_2O_3. For this, $Pb(NO_3)_2$ and Nb_2O_5 powders were taken as starting materials, with purities of 99% (Sigma-Aldrich) and 99.9% (Alfa Aesar), respectively. Eu_2O_3 powder

was used as a dopant with a purity of 99.9% (Alfa Aesar). $Pb(NO_3)_2$ and Nb_2O_5 powders were taken and mixed according to $PbNb_2O_6$ stoichiometry. Eu_2O_3 was subsequently added to this mixture in different molar ratios. Later on, these powder mixtures were homogenized by grinding in an agate mortar and subsequently sintered in an electric furnace at 1250 °C in an air atmosphere for 6 hours after pelleting. The crystalline phases of the ceramic samples were identified by X-ray diffractometry (XRD, Rigaku Corp., D-MAX 2200) using Cu-Kα radiation and Ni filter at a scanning rate of 2°/min between 20 and 65°. SEM observations were performed by SEM (FEI, Oregon, Inspect S50, USA). The elemental contents of the ceramic samples were examined by using an energy dispersive spectrometer (EDS, OXFORD Industries INCAxSight 7274; 133-eV resolution 5.9 keV)

which integrated to scanning electron microscope (SEM, JEOL Ltd., JSM-5910LV). The CL (cathodoluminescence) spectra were taken by a SEM (NOVA-NANOSEM 650), that is operated at 15 kV (spot size 3.5, work distance 6.6 mm, and high vacuum) equipped with field emission gun at room temperature. The CL system is equipped with a spectrometer (DATAN-Mono CL4), which allows monochromatic CL imaging as well as the acquisition of CL spectra on very localized spots of a sample. The absorptions of the samples were taken by a Perkin-Elmer Lambda spectrophotometer (USA).

RESULTS AND DISCUSSION

### Morphological and Structural Characterization
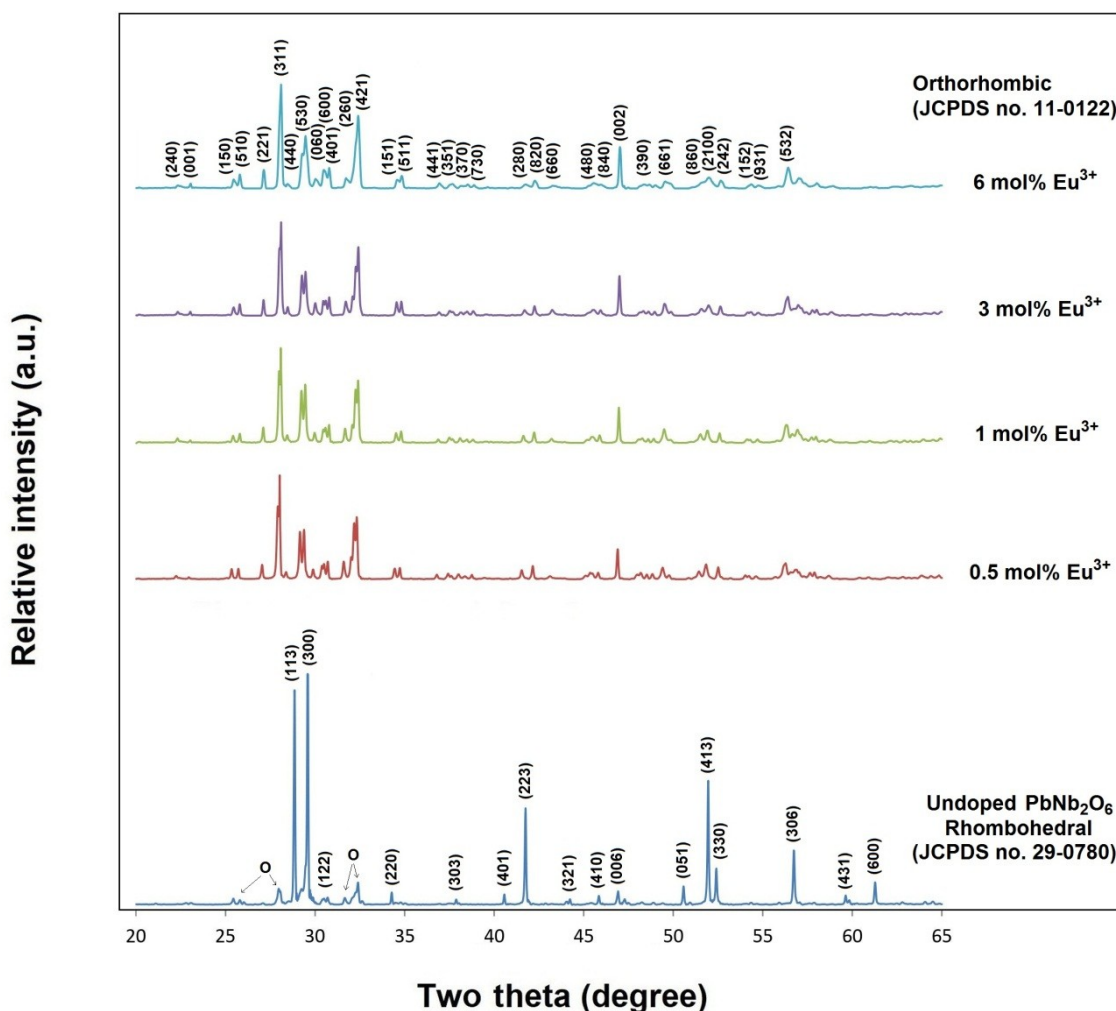
Figure 1: X-ray diffractions of undoped and Eu^{3+} doped $PbNb_2O_6$ samples.
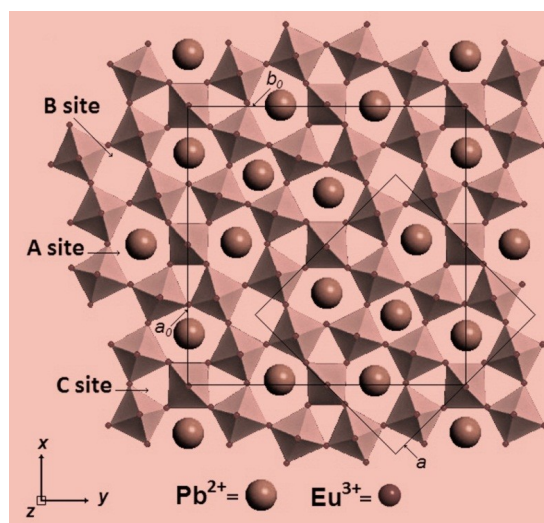
Figure 2: Relationship of orthorhombic and tetragonal in $PbNb_2O_6$ structure.

The results of X-Ray Diffraction for undoped and doped samples that sintered at 1250 °C for 6 hours are shown in Figure 1. XRD analysis also showed the undoped $PbNb_2O_6$ sample crystallized in rhombohedral (hexagonal) symmetry (JCPDS card No. 29–0780) with space group *R3/m* (no.160) while Eu^{3+} doped samples formed in orthorhombic symmetry (JCPDS card no. 11–0122) with space group *Cmm2* (no.35). The lattice parameters of rhombohedral were reported as $a = 10.501$ Å, $b = 10.501$ Å, $c = 11.555$ Å, $V = 1103$ Å^3 (28). The orthorhombic $PbNb_2O_6$ cell data have been reported as $a_0=17.65$ (Å), $b_0=17.91$ (Å) and $c_0=7.736$ (Å) (24). Interestingly, as seen from the XRD model of the $PbNb_2O_6$ samples, the Eu^{3+} doped samples changed to a different symmetry than the undoped sample. In the XRD pattern of the undoped sample, the rhombohedral phase, which normally crystallizes at 1150 °C, also formed at 1250 °C, and there is an orthorhombic phase indicated by "O" in the form of impurity in the rhombohedral phase. As stated in different studies (18,37), orthorhombic polymorph can be obtained by rapid cooling of tetragonal at temperatures between 1200-1250 °C. In this study, the average cooling rate is about 6 K/min, which is not sufficient for the transformation of the pure orthorhombic phase. However, the lack of rhombohedral polymorph with Eu^{3+} doping and the ease with which the orthorhombic polymorph was obtained indicate that an anisotropic phase transformation occurred as a result of thermal shock in the lattice caused by Eu^{3+} ions doping (18). The tetragonal ($a≈b,c$) and orthorhombic (a_0,b_0,c_0) polymorphs have tungsten bronze symmetry (24, 39, 40), where the lattice data of them are associated with $a_0=a\sqrt{2}$, $b_0≈a\sqrt{2}$, $c_0=2c$. Accordingly, the b/a ratio is approximately equal to 1.015 where a, b constants are fairly close. So, due to a small distortion in orthorhombic, the XRD pattern of the orthorhombic $PbNb_2O_6$ can be indexed based on tungsten bronze symmetry (24, 25). The relationship between orthorhombic and tetragonal polymorphs is illustrated in Figure 2, where tetragonal shows the small square and its corners located in the B tunnels, while orthorhombic represents the large square and its corners located in the octahedral sites (18).
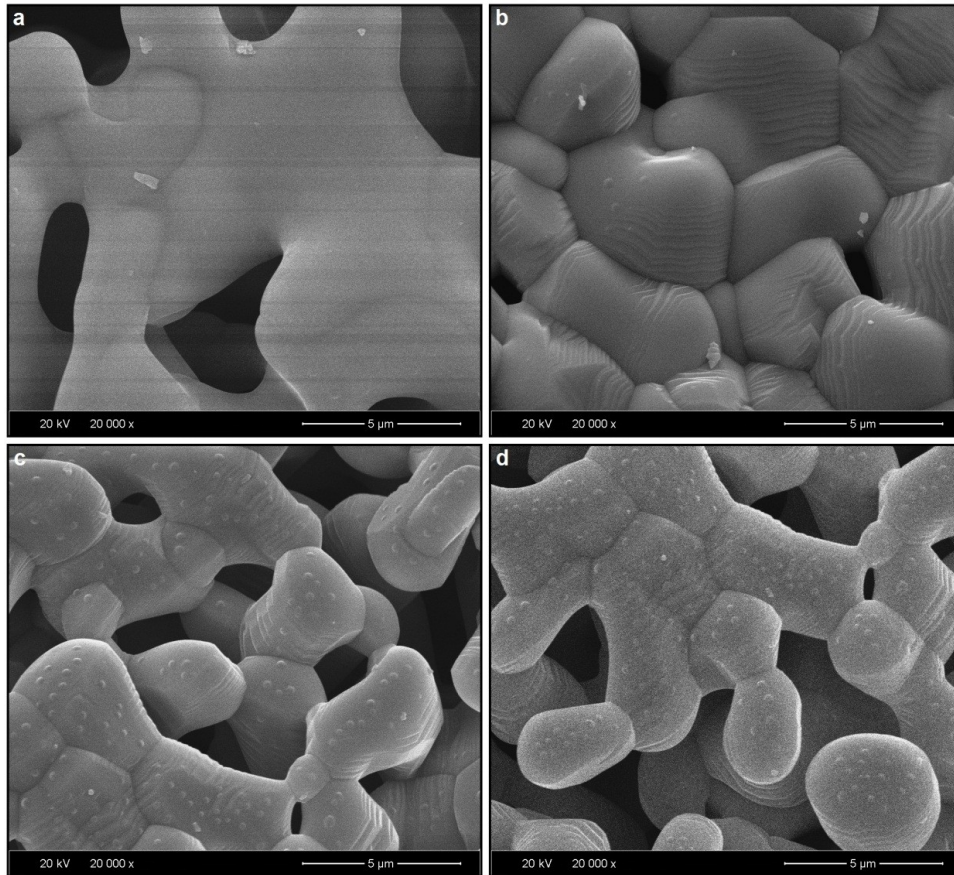
Figure 3: SEM micrographs of (a) undoped and (b) 0.5, (c) 3, (d) 6 mol% Eu^{3+} doped samples at 20 kV acceleration voltage, and 20.000x magnification.

SEM micrographs of undoped sample (rhombohedral) and 0.5, 3, 6 mol% Eu^{3+} doped ones (orthorhombic) are shown in Figure 3(a–d), respectively. The morphology of the grains was examined by the SEM. The grain morphology of the undoped sample showed smooth surface and an amorphous shape, while the boundaries of the grains were hard to see. Depending on concentration, the grain shapes of the doped samples exhibited an oval and wavy morphology, which are more common for 3 and 6 mol% samples. SEM findings uncovered a terraced morphology that can be ascribed to the angular structure of tungsten bronze. SEM results may also be associated with how morphological transformation between

orthorhombic and rhombohedral. The decrease in the grain size with the increase in Eu^{3+} concentration can be explained by the restriction of grain growth due to suppression in the lattice (41,42). The grain sizes for 0.5 and 6 mol% were detected between 3-11 and 1.5-6.5 µm, respectively.

EDS analysis was applied to the samples in order to define the composition change of the elements. EDS results (weight% and atomic%) for 6 mol% Eu^{3+} doped sample are given in Figure 4. As seen in the tabulated EDS results in Figure 4, the atomic% compositions of the elements are in agreement with the theoretical atomic amounts%.
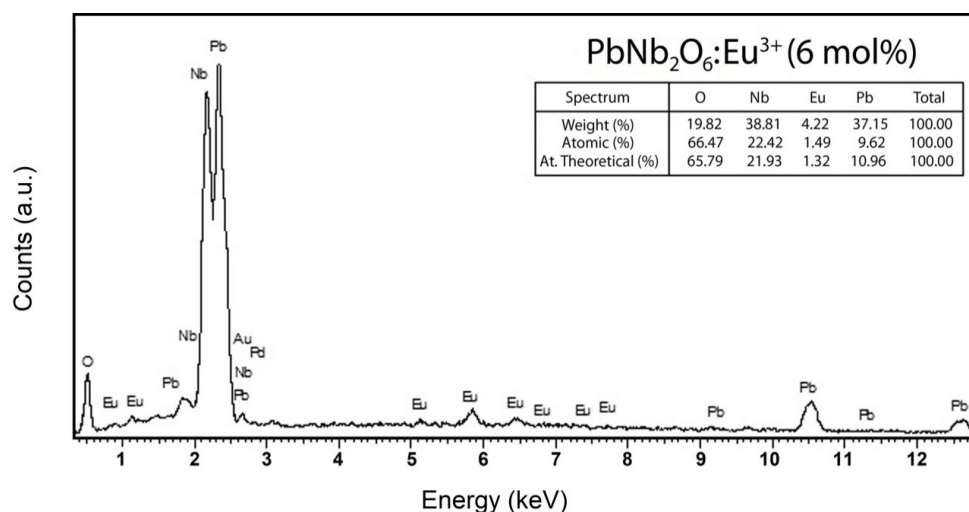
Figure 4: EDS spectrum and elemental analysis results (wt.%, at.%) and theoretical atomic percentages for 6 mol% Eu^{3+} doped sample.

Cathodoluminescence Analysis

Figure 5(a-e) shows the CL spectra of undoped $PbNb_2O_6$ (rhombohedral) and 0.5, 1, 3 and 6 mol% Eu^{3+} doped phosphors (orthorhombic) sintered at 1250 °C. In Fig. 4a, the CL spectrum of the undoped sample has a CL emission of around 640 nm. The observed CL emission of undoped $PbNb_2O_6$ is probably associated with the defect emission, which can be attributed to the recombination of electrons in the non-bridging oxygen band-gap state with holes in the valence band (43). Generally, considering lead niobate as a host structure, a weakness in CL emissions was observed. This is probably related to the presence of lead in the compound. Lead has the ability to stop gamma and X-ray radiation due to lead's high atomic number and stable isotopes (44).

A weak CL emission observed around 420 nm may probably be related to the rhombohedral host, and a peak around 440 nm observed in Eu^{3+} doped samples is associated with the orthorhombic polymorph. The illustration of rhombohedral $PbNb_2O_6$ structure is shown in Figure 6, where the rhombohedral has an edge-sharing crystal arrangement (28) while the orthorhombic (in Figure 2) has a corner-sharing structure. The edge-shared octahedral structure

is associated with a higher band gap compared to the corner-shared octahedral structure (45), which can be ascribed to a lower wavelength shift of rhombohedral or a larger wavelength shift of octahedral. Therefore, a change in wavelength is likely to occur with the rhombohedral-orthorhombic phase transformation, where the peak of the edge-shared rhombohedral host at about 420 nm, shifted to the peak of the corner-shared orthorhombic host at about 440 nm. The shift between the two polymorphs was also studied by absorption analysis, which is given in Figure 7. PL host absorption for rhombohedral $PbNb_2O_6$ has been previously reported around 385 nm (17), but it was not clearly observed in the same spectral range. The absorption peaks of the Eu^{3+} doped $PbNb_2O_6$ and undoped $PbNb_2O_6$ samples are around 370-375 nm. As seen in the spectral profiles, the absorption of the Eu^{3+} doped samples decreases with the increasing doping concentration. On the other hand, when compared to undoped and Eu^{3+} doped samples, it is seen that the undoped sample slightly shifts towards higher energy. Accordingly, based on the absorbance results where a slightly higher energy shift occurred, this supports the shift of rhombohedral host emission.
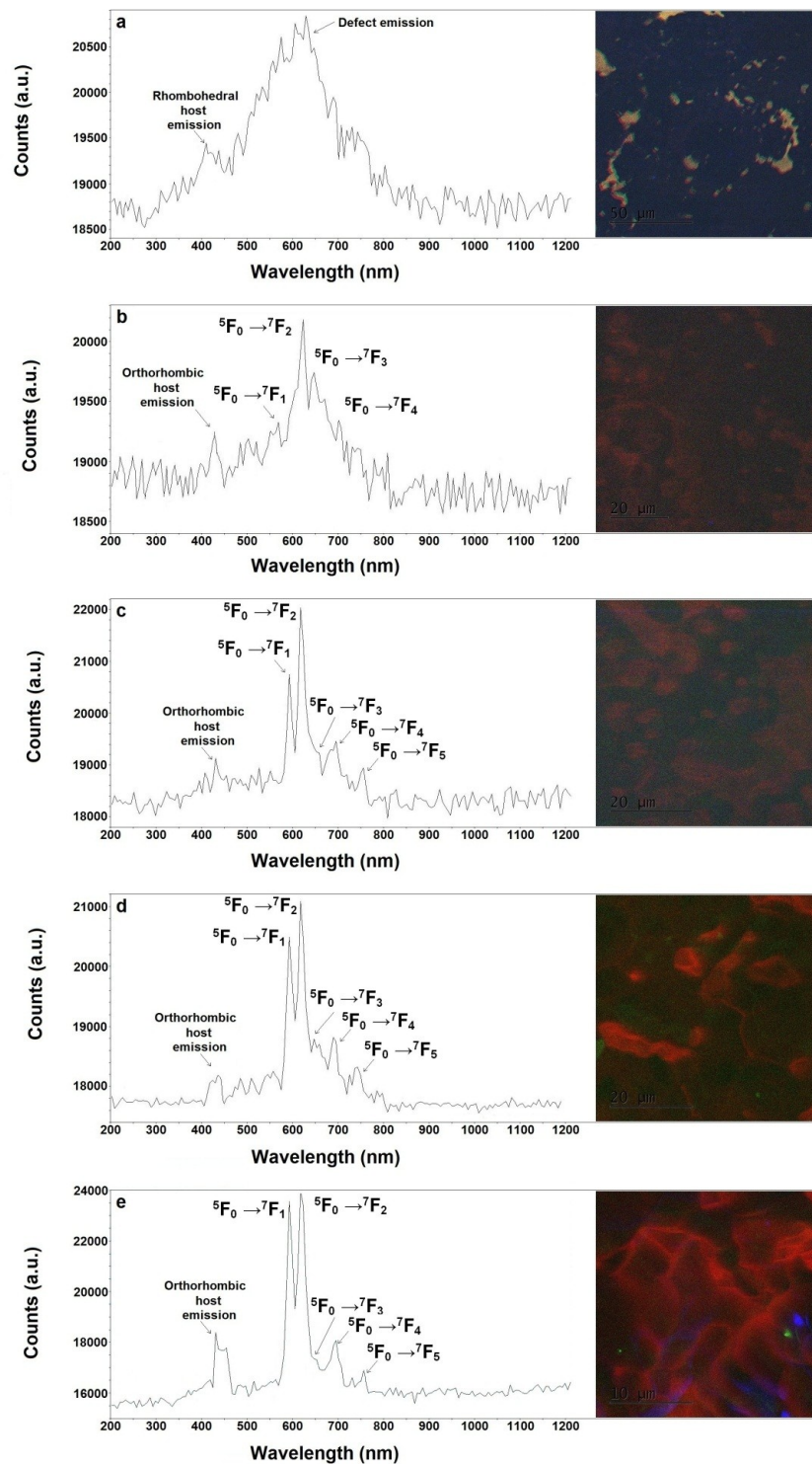
Figure 5: CL emission spectra and CL micrographs (inset figures) for (a) undoped $PbNb_2O_6$, and (b) 0.5, (c) 1, (d) 3, (e) 6 mol Eu^{3+} doped $PbNb_2O_6$ phosphors.
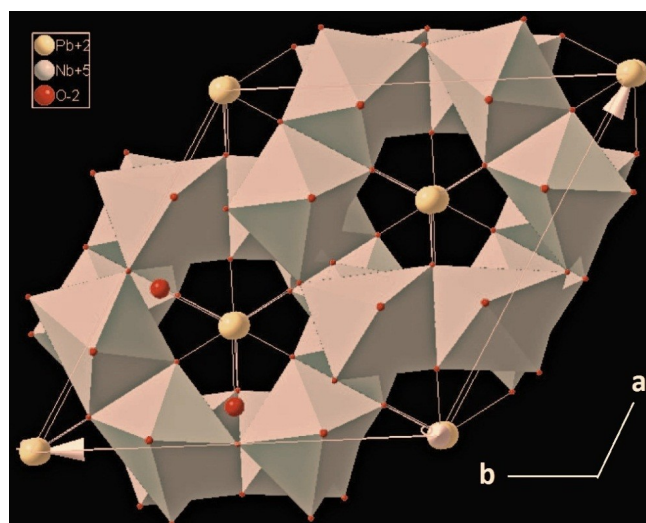
Figure 6: Illustration of rhombohedral (hexagonal) $PbNb_2O_6$ structure.

The CL emissions of Eu^{3+} doped phosphors were monitored for the CL peaks of 592, 618, 650, 695 and 755 nm corresponding to $^5F_0\rightarrow^7F_1$, $^5F_0\rightarrow^7F_2$, $^5F_0\rightarrow^7F_3$, $^5F_0\rightarrow^7F_4$, and $^5F_0\rightarrow^7F_5$ transitions, respectively. Increasing the Eu^{3+} concentration increased the $^5F_0\rightarrow^7F_J$ (J = 0, 1, 2, 3, 4, 5) transition intensities, while the highest CL intensity was reached at 6 mol% concentration. CL micrographs of undoped $PbNb_2O_6$ and Eu^{3+} doped phosphors are shown in the inset figures of Figure 4(a-e). As seen as in CL spectra, the asymmetry ratio ($^5F_0\rightarrow^7F_2/^5F_0\rightarrow^7F_1$) decreased or the symmetry of phosphor increased with increasing Eu^{3+} concentration. Among Eu^{3+} ion transitions, it is well known that the $^5D_0\rightarrow^7F_1$ magnetic dipole transition hardly changes with the crystal field around the Eu^{3+} ions whereas $^5D_0\rightarrow^7F_2$ electric dipole transition is very sensitive to the crystal field changes (42). In radioluminescence (RL) mechanism, the excitation of holes and electrons by high-energy X-rays may create asymmetry differences with the UV-Vis excitation mechanism of PL, where X-ray excitation with a volumetric character can change the asymmetric ratio due to its deeper penetration (46-48). On the basis of the similarity of the CL mechanism to the RL mechanism due to the high-energy electron beam, it is possible that electron beam irradiation changed the dipole moments in the Eu^{3+} doped host and caused the emission spectrum change. Therefore, when $PbNb_2O_6:Eu^{3+}$ phosphor was exposed to irradiation with high-energy electrons of CL, the symmetry of the Eu^{3+} local environment probably increased (46-48).
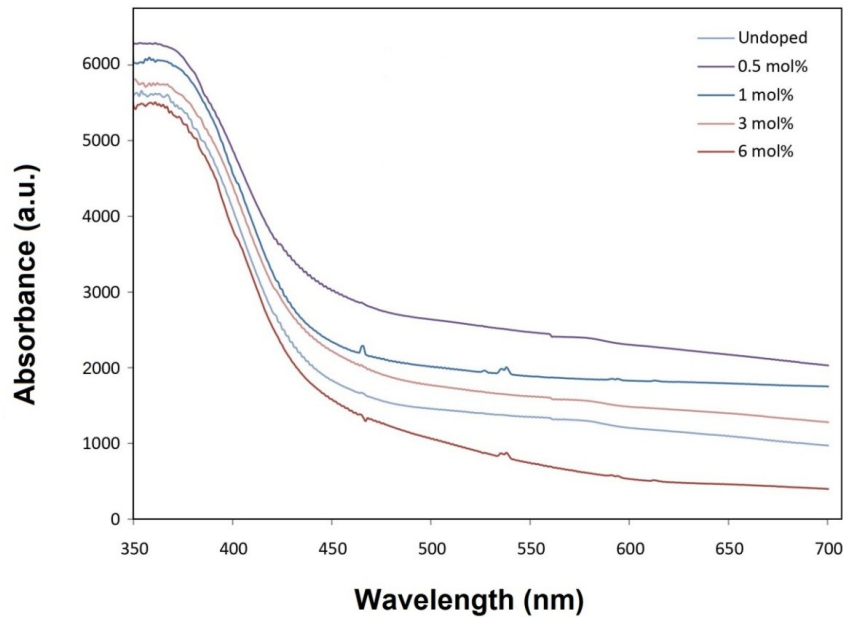
Figure 7: Absorption spectrums of undoped PbNb$_2$O$_6$ (rhombohedral) and Eu^{3+} doped PbNb$_2$O$_6$ (orthorhombic) samples.

In inset photographs of Figure 5(a-e), the CL micrograph of the undoped sample has different regions such as blue-yellow-green-red due to the broad peak between 400-800 nm, while the Eu^{3+} doped samples have red regions due to Eu^{3+} emissions. The UV lamp photographs of PbNb$_2$O$_6$ and PbNb$_2$O$_6$:Eu^{3+} phosphors under 254 nm are shown in Figure 8. The UV lamp photograph of the undoped sample has blue-violet emission that supports the peak around 420 nm. The Eu^{3+} doped samples with red color became brighter with increasing Eu^{3+} concentration, and 6 mol% doped sample has the brightest appearance, as seen in CL results, which show the highest emission intensity.
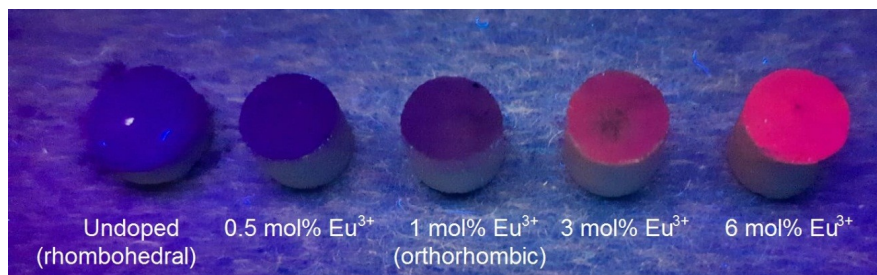
Figure 8: UV lamp photograph of undoped and Eu^{3+} doped PbNb$_2$O$_6$ ceramics phosphors with excitation of 254 nm or short wavelength.

CONCLUSION

By solid state reaction, Eu^{3+} doped orthorhombic PbNb$_2$O$_6$ phosphors with tugsten bronze symmetry were fabricated. According to X-ray diffraction results, undoped PbNb$_2$O$_6$ has a rhombohedral symmetry, while the Eu^{3+} presence between 0.5 and 6 mol% led to the orthorhombic phase transformation. SEM analysis revealed that the grains of the undoped sample have an amorphous shape and a smooth surface such that the boundary of grains is hardly seen. The grain shapes of Eu^{3+} doped samples for 3 and 6 mol% samples showed an oval and wavy morphology. CL emission of the undoped sample has a peak at around 640 nm, which is related to defect emission. The CL emission of rhombohedral PbNb$_2$O$_6$ host was not clearly observed in the CL spectral profiles. This can be associated with

the presence of lead in $PbNb_2O_6$, which has the ability to stop gamma and X-ray radiation. The rhombohedral-orthorhombic phase transformation led to a shift in the rhombohedral and orthorhombic CL host peaks, in which the edge-shared rhombohedral host and the corner-shared orthorhombic host have CL peaks at wavelengths of about 420 and 440 nm, respectively. The Eu^{3+} doped $PbNb_2O_6$ and undoped $PbNb_2O_6$ samples exhibited absorption peaks of around 370-375 nm, where the slightly higher energy of the undoped sample supports a high energy shift of the rhombohedral host emission. The CL emissions of $PbNb_2O_6{:}Eu^{3+}$ phosphors exhibited the $^5F_0{\rightarrow}^7F_J$ (J = 0, 1, 2, 3, 4, 5) characteristic transitions of Eu, and the highest CL intensity was observed at 6 mol% concentration. The decrease in the asymmetry ratio or the increase in magnetic dipole transition with the increase in doping concentration showed that the electron beam radiation of CL changes the dipole moments of the Eu^{3+} doped tungsten bronze host and causes a difference in the emission spectrum. UV lamp photograph of undoped $PbNb_2O_6$ exhibited blue-violet emission that supports the peak around 420 nm, while Eu^{3+} doped samples exhibited red color that became more evident with increasing Eu^{3+} concentration.

CONFLICT OF INTEREST

There is no conflict of interest.

REFERENCES

1. Ekmekçi MK, İlhan M, Güleryüz LF, Mergen A. Study on molten salt synthesis, microstructural determination and white light emitting properties of CoNb2O6:Dy3+ phosphor. Optik [Internet]. 2017 Jan [cited 2022 Oct 9];128:26–33. Available from: <URL>.

2. İlhan M, Ekmekçi MK, Keskin İÇ. Judd–Ofelt parameters and X-ray irradiation results of MNb 2 O 6 :Eu 3+ (M = Sr, Cd, Ni) phosphors synthesized via a molten salt method. RSC Adv [Internet]. 2021 [cited 2022 Oct 9];11(18):10451–62. Available from: <URL>.

3. Ekmekçi MK, İlhan M, Başak AS, Deniz S. Structural and Luminescence Properties of Sm3+ Doped TTB -Type BaTa2O6 Ceramic Phosphors. J Fluoresc [Internet]. 2015 Nov [cited 2022 Oct 9];25(6):1757–62. Available from: <URL>.

4. İlhan M, Ekmekçi MK, Oraltay RG, Başak AS. Structural and Near-Infrared Properties of Nd3+ Activated Lu3NbO7 Phosphor. J Fluoresc [Internet].

2017 Jan [cited 2022 Oct 9];27(1):199–203. Available from: <URL>.

5. İlhan M, Ekmekçi MK, Mergen A, Yaman C. Photoluminescence characterization and heat treatment effect on luminescence behavior of BaTa 2 O 6 :Dy 3+ phosphor. Int J Appl Ceram Technol [Internet]. 2017 Nov [cited 2022 Oct 9];14(6):1134–43. Available from: <URL>.

6. Ekmekçi MK, Erdem M, Başak AS, İlhan M, Mergen A. Molten salt synthesis and optical properties of Eu3+, Dy3+or Nd3+ doped NiNb2O6 columbite-type phosphors. Ceramics International [Internet]. 2015 Sep [cited 2022 Oct 9];41(8):9680–5. Available from: <URL>.

7. Ekmekçi MK, Erdem M, Başak AS. Molten salt synthesis, visible and near-IR region spectral properties of europium or neodymium doped CoNb 2 O 6 columbite niobate. Dalton Trans [Internet]. 2015 [cited 2022 Oct 9];44(12):5379–85. Available from: <URL>.

8. İlhan M. Synthesis, Structural Properties and Visible–Near Infrared Photoluminescence of Trivalent Erbium (Er3+) Doped BaTa2O6 Phosphor. AKU-J Sci Eng [Internet]. 2017 Aug 1 [cited 2022 Oct 9];17(2):675–82. Available from: <URL>.

9. Ekmekçi MK, İlhan M, Ege A, Ayvacıklı M. Microstructural and Radioluminescence Characteristics of Nd3+ Doped Columbite-Type SrNb2O6 Phosphor. J Fluoresc [Internet]. 2017 May [cited 2022 Oct 9];27(3):973–9. Available from: <URL>.

10. Binnemans K. Interpretation of europium(III) spectra. Coordination Chemistry Reviews [Internet]. 2015 Jul [cited 2022 Oct 9];295:1–45. Available from: <URL>.

11. Mitsui T, Yamamoto N, Tadokoro T, Ohta S. Cathodoluminescence image of defects and luminescence centers in ZnS/GaAs(100). Journal of Applied Physics [Internet]. 1996 Dec 15 [cited 2022 Oct 9];80(12):6972–9. Available from: <URL>.

12. Yacobi BG, Holt DB. Cathodoluminescence scanning electron microscopy of semiconductors. Journal of Applied Physics [Internet]. 1986 Feb 15 [cited 2022 Oct 9];59(4):R1–24. Available from: <URL>.

13. İlhan M, Güleryüz LF. Cathodoluminescence and photoluminescence of BaTa2O6:Sm3+ phosphor depending on the sintering temperature. Chem Pap [Internet]. 2022 Jul 31 [cited 2022 Oct 9]; Available from: <URL>.

14. Edwards PR, Martin RW. Cathodoluminescence nano-characterization of semiconductors. Semicond Sci Technol [Internet]. 2011 Jun 1 [cited 2022 Oct 9];26(6):064005. Available from: <URL>.

15. Dierre B, Yuan X, Sekiguchi T. Low-energy cathodoluminescence microscopy for the characterization of nanostructures. Science and Technology of Advanced Materials [Internet]. 2010 Feb [cited 2022 Oct 9];11(4):043001. Available from: <URL>.

16. Ma DDD, Lee ST, Mueller P, Alvarado SF. Scanning Tunneling Microscope Excited Cathodoluminescence from ZnS Nanowires. Nano Lett [Internet]. 2006 May 1 [cited 2022 Oct 9];6(5):926–9. Available from: <URL>.

17. İlhan M, Ekmekçi MK, Demir A, Demirer H. Synthesis and Optical Properties of Novel Red-Emitting PbNb2O6: Eu3+ Phosphors. J Fluoresc [Internet]. 2016 Sep [cited 2022 Oct 9];26(5):1637–43. Available from: <URL>.

18. İlhan M, Keskin İÇ. Evaluation of structural behaviour, radioluminescence, Judd-Ofelt analysis and thermoluminescence kinetic parameters of Eu3+ doped TTB–type lead metaniobate phosphor. Physica B: Condensed Matter [Internet]. 2020 May [cited 2022 Oct 9];585:412106. Available from: <URL>.

19. Başak AS, Ekmekçi MK, Erdem M, Ilhan M, Mergen A. Investigation of Boron-doping Effect on Photoluminescence Properties of CdNb2O6: Eu3+ Phosphors. J Fluoresc [Internet]. 2016 Mar [cited 2022 Oct 9];26(2):719–24. Available from: <URL>.

20. Francombe MH. Polymorphism in lead metaniobate. Acta Cryst [Internet]. 1956 Aug 1 [cited 2022 Oct 9];9(8):683–4. Available from: <URL>.

21. Roth RS, Waring JL. Phase equilibrium relations in the binary system barium oxide-niobium pentoxide. J RES NATL BUR STAN SECT A [Internet]. 1961 Jul [cited 2022 Oct 9];65A(4):337. Available from: <URL>.

22. Xiao Q, Zhou Q, Zhang J, Ouyang L. Photocatalytic decolorization of methylene blue over monoclinic pyrochlore-type Pb2Nb2O7 under visible light irradiation. Journal of Alloys and Compounds [Internet]. 2009 Jan [cited 2022 Oct 9];468(1–2):L9–12. Available from: <URL>.

23. Sahini MG, Grande T, Fraygola B, Biancoli A, Damjanovic D, Setter N. Solid Solutions of Lead Metaniobate-Stabilization of the Ferroelectric Polymorph and the Effect on the Lattice Parameters, Dielectric, Ferroelectric, and Piezoelectric Properties. Viehland D, editor. J Am Ceram Soc [Internet]. 2014 Jan [cited 2022 Oct 9];97(1):220–7. Available from: <URL>.

24. Francombe MH, Lewis B. Structural, dielectric and optical properties of ferroelectric lead metaniobate. Acta Cryst [Internet]. 1958 Oct 1 [cited 2022 Oct 9];11(10):696–703. Available from: <URL>.

25. Subbarao EC, Shirane G, Jona F. X-ray dielectric, and optical study of ferroelectric lead metatantalate and related compounds. Acta Cryst [Internet]. 1960 Mar 1 [cited 2022 Oct 9];13(3):226–31. Available from: <URL>.

26. Goodman G. Ferroelectric Properties of Lead Metaniobate. J American Ceramic Society [Internet]. 1953 Nov [cited 2022 Oct 9];36(11):368–72. Available from: <URL>.

27. Subbarao EC. X-Ray Study of Phase Transitions in Ferroelectric PbNb2O6 and Related Materials. J American Ceramic Society [Internet]. 1960 Sep [cited 2022 Oct 9];43(9):439–42. Available from: <URL>.

28. Chakraborty KR, Sahu KR, De A, De U. Structural Characterization of Orthorhombic and Rhombohedral Lead Meta-Niobate Samples. Integrated Ferroelectrics [Internet]. 2010 Nov 12 [cited 2022 Oct 9];120(1):102–13. Available from: <URL>.

29. Haertling GH. Ferroelectric Ceramics: History and Technology. Journal of the American Ceramic Society [Internet]. 1999 Apr [cited 2022 Oct 9];82(4):797–818. Available from: <URL>.

30. Sahu KR, De U. Thermal characterization of piezoelectric and non-piezoelectric Lead Meta-Niobate. Thermochimica Acta [Internet]. 2009 Jun [cited 2022 Oct 9];490(1–2):75–7. Available from: <URL>.

31. Sahu KR, De U. Impedance Spectroscopy of Piezoelectric 0.963PbNb2O6 – 0.037Ca0.6TiO3. Materials Today: Proceedings [Internet]. 2019 [cited 2022 Oct 9];11:859–68. Available from: <URL>.

32. Fang R, Zhou Z, Liang R, Dong X. Effects of CuO addition on the sinterability and electric properties in PbNb2O6-based ceramics. Ceramics International [Internet]. 2020 Oct [cited 2022 Oct 9];46(15):23505–9. Available from: <URL>.

33. Yu H, Liu Y, Deng C, Xia M, Zhang X, Zhang L, et al. Lithium storage behaviors of PbNb2O6 in rechargeable batteries. Ceramics International [Internet]. 2021 Oct [cited 2022 Oct 9];47(19):26732–7. Available from: <URL>.

34 Yoel A, Michael PEP, Kokate MV, Tabhane VA. Effect of gamma rays irradiation on ferroelectric phase transition and domain defect interaction in lead meta niobate single crystal. Physica B: Condensed Matter [Internet]. 2012 Feb [cited 2022 Oct 9];407(4):576–80. Available from: <URL>.

35. Raghavendra V, Viswarupachary P, Suryanarayana B, Chandra Mouli K, Vikram GNVR, Murali N. Dielectric and piezoelectric properties of Sm3+ doped lead barium niobate (PBN) ceramics. Physica B: Condensed Matter [Internet]. 2019 Mar [cited 2022 Oct 9];556:75–81. Available from: <URL>.

36. Aslam S, Rafique HM, Ramay SM, Akhtar N, Mustafa GM, Siddig AA, et al. Tuning the dielectric properties of PbNb2O6 perovskite through calcium substitution. Physica B: Condensed Matter [Internet]. 2022 Jun [cited 2022 Oct 9];635:413840. Available from: <URL>.

37. Li YM, Cheng L, Gu XY, Zhang YP, Liao RH. Piezoelectric and dielectric properties of PbNb2O6-based piezoelectric ceramics with high Curie temperature. Journal of Materials Processing Technology [Internet]. 2008 Feb [cited 2022 Oct 9];197(1–3):170–3. Available from: <URL>.

38. Guerrero F, Leyet Y, Venet M, de Los S. Guerra J, Eiras JA. Dielectric behavior of the PbNb2O6 ferroelectric ceramic in the frequency range of 20Hz to 2GHz. Journal of the European Ceramic Society [Internet]. 2007 Jan [cited 2022 Oct 9];27(13–15):4041–4. Available from: <URL>.

39. Neurgaonkar RR, Cory WK. Progress in photorefractive tungsten bronze crystals. J Opt Soc Am B [Internet]. 1986 Feb 1 [cited 2022 Oct 9];3(2):274. Available from: <URL>.

40. Xu Y. Ferroelectric tungsten-bronze-type niobate crystals. In: Ferroelectric materials and their applications [Internet]. Amsterdam ; New York : New York, NY, USA: North-Holland ; Sole distributors for the USA and Canada, Elsevier Science Pub. Co; 1991. p. 247–9. Available from: <URL>.

41. İlhan M, Keskin İÇ, Gültekin S. Assessing of Photoluminescence and Thermoluminescence Properties of Dy3+ Doped White Light Emitter TTB-Lead Metatantalate Phosphor. Journal of Elec Materi [Internet]. 2020 Apr [cited 2022 Oct 9];49(4):2436–49. Available from: <URL>.

42. İlhan M, Ekmekçi MK, Mergen A, Yaman C. Synthesis and Optical Characterization of Red-Emitting BaTa2O6:Eu3+ Phosphors. J Fluoresc

[Internet]. 2016 Sep [cited 2022 Oct 9];26(5):1671–8. Available from: <URL>..

43. Coenen T, Haegel NM. Cathodoluminescence for the 21st century: Learning more from light. Applied Physics Reviews [Internet]. 2017 Sep [cited 2022 Oct 9];4(3):031103. Available from: <URL>.

44. Li Z, Zhou W, Zhang X, Gao Y, Guo S. High-efficiency, flexibility and lead-free X-ray shielding multilayered polymer composites: layered structure design and shielding mechanism. Sci Rep [Internet]. 2021 Dec [cited 2022 Oct 9];11(1):4384. Available from: <URL>.

45. Kamminga ME, de Wijs GA, Havenith RWA, Blake GR, Palstra TTM. The Role of Connectivity on Electronic Properties of Lead Iodide Perovskite-Derived Compounds. Inorg Chem [Internet]. 2017 Jul 17 [cited 2022 Oct 9];56(14):8408–14. Available from: <URL>.

46. İlhan M, Katı Mİ, Keskin İÇ, Güleryüz LF. Evaluation of structural and spectroscopic results of tetragonal tungsten bronze MTa2O6:Eu3+ (M = Sr, Ba, Pb) phosphors and comparison on the basis of Judd-Ofelt parameters. Journal of Alloys and Compounds [Internet]. 2022 Apr [cited 2022 Oct 9];901:163626. Available from: <URL>.

47. İlhan M, Keskin İÇ, Güleryüz LF, Katı Mİ. A comparison of spectroscopic properties of Dy3+-doped tetragonal tungsten bronze MTa2O6 (M = Sr, Ba, Pb) phosphors based on Judd–Ofelt parameters. J Mater Sci: Mater Electron [Internet]. 2022 Jul [cited 2022 Oct 9];33(20):16606–20. Available from: <URL>.

48. İlhan M, Keskin İÇ. Analysis of Judd–Ofelt parameters and radioluminescence results of SrNb 2 O 6 :Dy 3+ phosphors synthesized via molten salt method. Phys Chem Chem Phys [Internet]. 2020 [cited 2022 Oct 9];22(35):19769–78. Available from: <URL>.